J. Fluid Mech. (2006), *vol.* 551, *pp.* 49–62.
doi:10.1017/S0022112005007901 Printed in the United Kingdom

Hysteretic gravity-wave bifurcation in a highly turbulent swirling flow

By NICOLÁS MUJICA[1,2] AND DANIEL P. LATHROP[1]

[1]Department of Physics, IREAP and IPST, University of Maryland, College Park, MD 20742, USA

[2]Departamento de Física, Facultad de Ciencias Físicas y Matemáticas, Universidad de Chile, Avenida Blanco Encalada 2008, Santiago, Chile

(Received 27 February 2005 and in revised form 6 September 2005)

We report on experimental observations of a gravity-wave instability forced by a highly turbulent free-surface Taylor–Couette flow. Bistability and hysteresis are observed at the bifurcation from a turbulent base state, with an axisymmetric mean flow, to a turbulent gravity-wave state, with an azimuthal $m = 1$ pattern related to the mean flow and free surface. We show that the critical Reynolds number at which the wave state appears is not sharply defined as it depends on turbulent fluctuations.

1. Introduction

Many nonlinear systems present transitions that are affected by the presence of noise or fluctuations. Of particular interest are bifurcations that occur when the system is forced by a fluctuating field. Magnetohydrodynamic examples are the dynamo and magnetorotational instabilities observed in liquid metals, where the velocity field is highly turbulent at the instability onset (see for example Fauve & Pétrélis 2003 and Sisan *et al.* 2004). The role of turbulent fluctuations in these systems seems unclear, and is in some cases twofold as discussed by Marié *et al.* (2002). For example, recent constrained dynamo experiments show that fluctuations are not necessary to explain the onset value of the relevant control parameter – knowledge of the mean flow suffices – although they do give the correct saturation magnetic field value (Pétrélis & Fauve 2001). In the field of fluid mechanics, the existence of finite-wavelength instabilities in turbulent flows is puzzling. Prigent *et al.* (2002) report experiments on both plane Couette and Taylor–Couette flow that show finite-wavelength modulations of their basic turbulent flows. In a recent paper Ravelet *et al.* (2004) present experiments on a highly turbulent von Kármán flow that show a hysteretic bifurcation for $Re \sim 10^5$. The exchange of stability occurs between mean flows of different average symmetry, which are actually never realized at any given time. These results are striking because although bifurcations and symmetry breaking occur on the route to turbulence, in the limit $Re \to \infty$ the flow is expected to recover the system basic symmetries (see Frisch 1995). In some aspects these systems behave as low-dimensional dynamical systems, although they present novel statistics at the transition as discussed by Ravelet *et al.* (2004). More generally, the question of multiple solutions in laminar or turbulent flows remains open. At low Re, up to 25 different laminar states in Taylor–Couette flow for a given rotation rate have been reported by Coles (1965). Other examples of systems that present hysteresis and finite-amplitude instabilities are tornadoes (Shtern & Hussain 1993), vortex breakdown (Billant, Chomaz & Huerre 1998), and flows above delta-wings and in diverging tubes (for a review see Shtern & Hussain 1999).

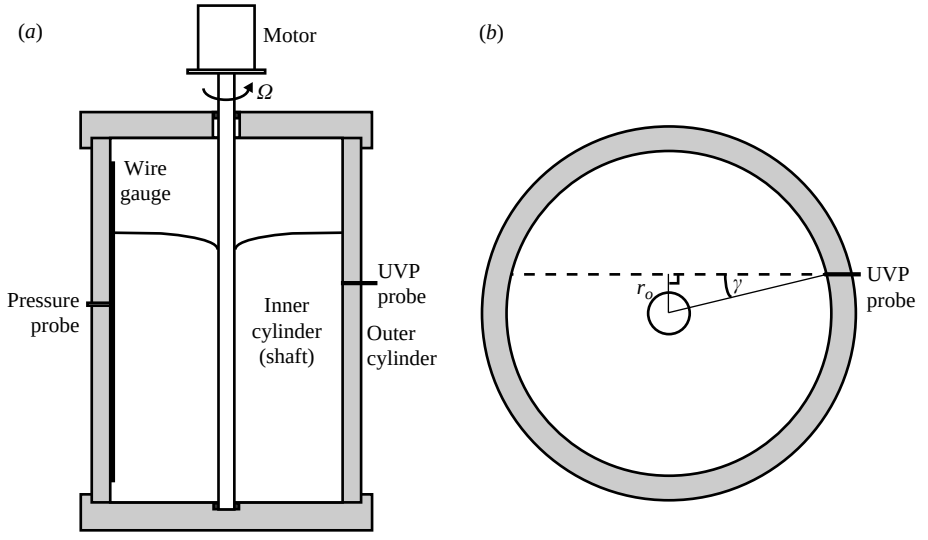

FIGURE 1. (*a*) Schematic drawing of the Taylor–Couette apparatus, partially filled with distilled water. The Plexiglas outer cylinder is stationary and the stainless steel inner cylinder rotates at an angular rotation rate Ω. Also shown are the wire gauge for liquid level measurements and both the pressure and ultrasound velocimetry profiling (UVP) probes. (*b*) Top view showing the UVP geometry. The dashed line shows the ultrasonic beam direction, at angle with respect to the outer wall normal of $\gamma = 13.6 \pm 0.5°$. The minimum cylindrical radius that can be probed is $r_o = 5.2 \pm 0.2$ cm.

In this paper we report the experimental study of a transition observed in a free-surface Taylor–Couette flow at $Re \sim 10^6$. A highly turbulent base state, for which the mean flow is axisymmetric and thus respects on average the symmetries of the driving apparatus, bifurcates to a turbulent gravity-wave state, with a mean flow (averaged in a frame rotating with the wave) that has an azimuthal wavenumber $m = 1$. The instability is a first-order transition in the sense that it is not a continuous one. Accordingly, it presents bistability and hysteresis. In the bistable range of parameters one needs the correct form and level of disturbance to observe the transition. The wave state grows from a resonant mode of the free surface and gets its energy from the turbulent background flow. Turbulence is important in the observed transition in several ways. The transition is noise driven, the main source of noise being the turbulent fluctuations. In addition, the base state from which the wave state grows has its properties, including the mean velocity field, determined by turbulence. Finally, it may be possible that the properties of the inner cylinder turbulent boundary layer drive the instability, as in other instabilities observed in swirling flows (Shtern & Hussain 1999).

This paper is organized as follows: The experimental setup is presented in § 2, and the relevant dimensionless parameters are briefly discussed in § 3. We present the experimental results on the base-state characterization and the gravity-wave bifurcation in § 4. The paper ends with a discussion and conclusions in § 5.

2. Experimental setup

The Taylor–Couette apparatus is schematically presented in figure 1(*a*). The outer cylinder is Plexiglas with inner radius $b = 22.1$ cm and a thickness of 3.34 cm. The

axial length of the available working volume is $L = 69.5$ cm. The setup is the same as used in Lathrop, Fineberg & Swinney (1992), except that the inner stainless steel cylinder is of smaller radius, $a = 2.83$ cm, which is concentric with respect to the outer one within 0.013 cm. The working fluid is distilled water, with the temperature $T = 24 \pm 1\,^{\circ}$C. Three different quiescent water levels h_o are studied, $h_o = 34$, 42 and 50 cm. The system is filled using a pump to transfer water from a reservoir. A 2 kW servomotor drives the inner cylinder, with an accuracy of 1% in rotation rate. The inner cylinder rotation rate $F = \Omega/2\pi$ is varied in the range 3.6–33 Hz and the outer cylinder is stationary.

The base-state velocity field is characterized with an ultrasonic velocimetry profiling technique (UVP) first developed by Takeda (1991) and by imaging of the surface profile. In addition, both the turbulent base state and the gravity-wave state are characterized by a wall pressure probe, located at 30 cm above the bottom plate.

The velocity measurements were obtained using pulsed ultrasound Doppler velocimetry at 4 MHz. The ultrasonic probe position and beam geometry are presented in figure 1(*b*). The angle with respect to the outer wall normal, γ, is chosen to be small enough so that we can probe near the inner cylinder, but has to be large enough to avoid reflections from it. We stress that this technique gives access to both the radial and azimuthal components of the mean velocity field, given the condition that one can measure velocity profiles along the total length of the acoustic beam (Sisan *et al.* 2004).

The local surface amplitude disturbance, δh, is determined near the outer cylinder by a wire gauge, which measures the voltage drop V_w, and thus the resistance R_w, between two thin stainless steel rods. The wire gauge resistance measurements are performed by adding a $R_o = 100\,\mathrm{k}\Omega$ resistance in series and by measuring the voltage drop V_w across the two rods with a lock-in amplifier, which drives the total circuit at 2 kHz with a r.m.s. amplitude $V_o = 2$ V. In general, R_w is related to V_w by $R_n = V_n/(1 - V_n)$, where $R_n = R_w/R_o \ll 1$ and $V_n = V_w/V_o \ll 1$ are their normalized values. The stainless steel rods are 0.8 mm in diameter and 60 cm in length, separated by four uniformly placed nylon spacers of 3 mm. This wire gauge is placed radially, such that both rods are at the same azimuthal angle with respect to the rotation axis, and it is immersed 5 cm above the bottom plate. After proper calibration, it is possible to relate δh to the resistance measurement R_w. We note that due to contamination, water conductivity increases and R_w slowly decreases with time. Typical changes are of 1 % for a 1 hour period. In order to have absolute values of surface disturbance amplitude, periodic quiescent water level resistance measurements are performed.

Typical bifurcation study runs consist of two rotation rate ramps: increasing and decreasing F. For increasing F, 24 min time series of wire gauge voltage V_w and wall pressure p_w are recorded. Near (respectively far from) the transitions values, F increases by 0.4 Hz steps (respectively 0.8 Hz). For fixed F, each time series acquisition starts from quiescent distilled water, with 8 min settling down time between each rotation rate. The decreasing ramps start at the maximum F at which the increasing ramp ends. In this case the time series are of 5 min duration, without stopping the motor between each rotation rate.

Finally, except for the ultrasonic data, both wire gauge and pressure signals are transferred and stored on a computer, at a sampling rate of 200 Hz. For velocity profile measurements of the base state the cylinder is completely filled with water, in order to avoid the presence of bubbles in the flow. Indeed, even for runs with a free surface at moderate F, bubbles are pulled down from the liquid/gas interface, spiralling around the inner cylinder and are eventually ejected into the bulk of the

fluid. Hollow glass spheres are added into the fluid as ultrasound tracer particles, of mean density $0.75\,\mathrm{g\,cm^{-3}}$ and mean size $140\,\mu\mathrm{m}$, at a volume fraction of 1×10^{-4}.

3. Relevant dimensionless parameters

Our system is described by the group of eight parameters:

$$\rho,\ \nu,\ g,\ \sigma,\ U,\ L,\ a,\ h_o. \tag{3.1}$$

Here, ρ and ν are the fluid density and kinematic viscosity respectively, g the gravitational acceleration, and σ is the water/air interface surface tension. Finally, $U=a\Omega$ and $L=b-a$ are the typical velocity and length scales. For this group there are three physical units (length, time and mass). The system is therefore described by five independent dimensionless parameters:

(i) Reynolds number, Re, defined as the ratio of inertial and viscous forces. The corresponding integral Reynolds number, $Re=\Omega a(b-a)/\nu$, is in the range 1.23×10^5–1.13×10^6. The flow is then strongly turbulent.

(ii) Capillary number, Ca, defined as the ratio of viscous and surface tension forces: $Ca=\rho\nu U/\sigma$. Taking $\sigma\approx70\,\mathrm{mN\,m^{-1}}$, Ca varies in the range 9.1×10^{-3}–8.4×10^{-2}. This is only a rough estimate as we have used the value for σ corresponding to a clean water/air interface.

(iii) Froude number, Fr, defined as the ratio of inertial forces and gravity: $Fr=U^2/gL$, which varies in the range 0.2–17.9. Notice that for $Fr\sim O(1)$ we expect an interplay between inertia and gravity leading to wave-like behaviour.

(iv) The last two parameters are h_o/L and a/L, giving aspect ratio $h_o/(b-a)=1.8$, 2.2 and 2.6 for $h_o=34$, 42 and 50 cm respectively, and radius ratio $a/b=0.128$.

For our current setup only two parameters are independently controlled, F and h_o. Thus, we choose to describe the system with the parameters Re and h_o/L.

4. Experimental results

4.1. *Base-state characterization*

In this section we present a characterization of the azimuthal component of the basic flow. We focus on this component because it is the dominant one, the radial component being at maximum about 10% of the azimuthal one. The axial component has not been measured. Visual observations indicate that it is small too, except perhaps very close to the inner cylinder and near the top surface. Thus, this is not a full characterization of the basic state. In addition, in order to avoid the presence of bubbles in the bulk of the fluid, the working volume is completely filled with water during the velocimetry data acquisition. This is an estimation of only the bulk azimuthal flow. By comparing the measured azimuthal component with surface profile measurements we conclude that: (i) the azimuthal component is indeed dominant, (ii) the mean angular momentum is constant in the bulk of the flow.

Below the critical value at which the bifurcation occurs, we observe that for a large range of Reynolds numbers the mean flow has the symmetries of the driving apparatus, as expected for highly turbulent flows (Frisch 1995). Indeed, the measured mean azimuthal flow is axisymmetric and, moreover, the mean angular momentum is constant in the bulk of the flow (see figure 2). This implies that except in the boundary layers, the mean flow obeys $\boldsymbol{v}\approx Ar^{-1}\hat{\boldsymbol{\theta}}$ in cylindrical coordinates, where A is constant and r is the cylindrical radius. A regression fit of the form $v_\theta\sim r^{-\alpha}$, performed with the data presented in figure 2 for $r<15\,\mathrm{cm}$, gives $\alpha=0.97\pm0.05$. We remark

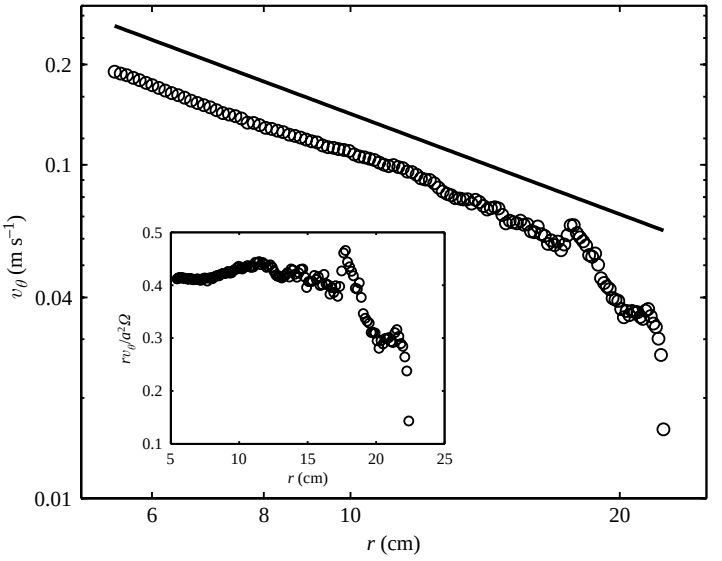

FIGURE 2. Base-state mean azimuthal velocity profile in $\log_{10}$-$\log_{10}$ scale, obtained from 1024 profiles, for $F = 5$ Hz ($Re \approx 1.71 \times 10^5$). The continuous line shows the slope -1. The inset shows the mean normalized angular momentum profile. To avoid the presence of bubbles in the bulk of the fluid, the working volume is completely filled with water (no liquid/air interface). Similar results were obtained for higher F, up to 30 Hz.

that near the inner cylinder a weak downward axial flow is also observed, although we have not yet measured its magnitude. It is evidenced by the presence of spiral vortices where air bubbles concentrate, which are eventually expelled into the bulk once the vortex loses intensity.

Another characterization of the base state is given through analysis of the surface profile. We present in figure 3(a) an image of the base-state free surface near the inner cylinder, for $h_o = 50$ cm and $F = 20$ Hz ($Re = 6.85 \times 10^5$). Due to centrifugal forces, the free surface deforms quite strongly, up to 5 cm at the inner cylinder. Away from the boundaries, this deformation follows a power law behaviour $\eta \sim r^{-\beta}$, with β in the range 1.9–2.0. Using Bernoulli's law, it is possible to show that we should have $\beta \approx 2\alpha$, as we indeed observe.

Even at low rotation rates, fluctuations in the flow cause the free surface to exhibit small-amplitude waves. These waves are dominated by the fundamental surface wave mode, which corresponds to an azimuthal wavenumber $m = 1$. This is easily observable by simple visual inspection, as indicated in figure 3(a) by an horizontal white dashed line; a temporal Fourier analysis of δh confirms this. These surface perturbations increase in amplitude as we increase F, although they do not present long-time coherence (see figure 4a, c). The same can be said for the structure of the free surface at the inner cylinder: this interface first presents turbulent fluctuations and, as we increase F, spatially coherent perturbations are observed. The latter are also dominated by an azimuthal wavenumber $m = 1$, as shown in figure 3(a) by a white arrow. They also increases in amplitude as we increase F and they do not have long-time coherence. The $m = 1$ resonant structure becomes observable at moderate rotation rates, say above 10 Hz, that is for $Re \gtrsim 3.42 \times 10^5$. Notice that for $F = 10$ Hz, $F_r \approx 1.65$. Finally, we note that small-amplitude, short-wavelength surface spiral waves are also observed, which are generated at the inner cylinder. These spiral waves are

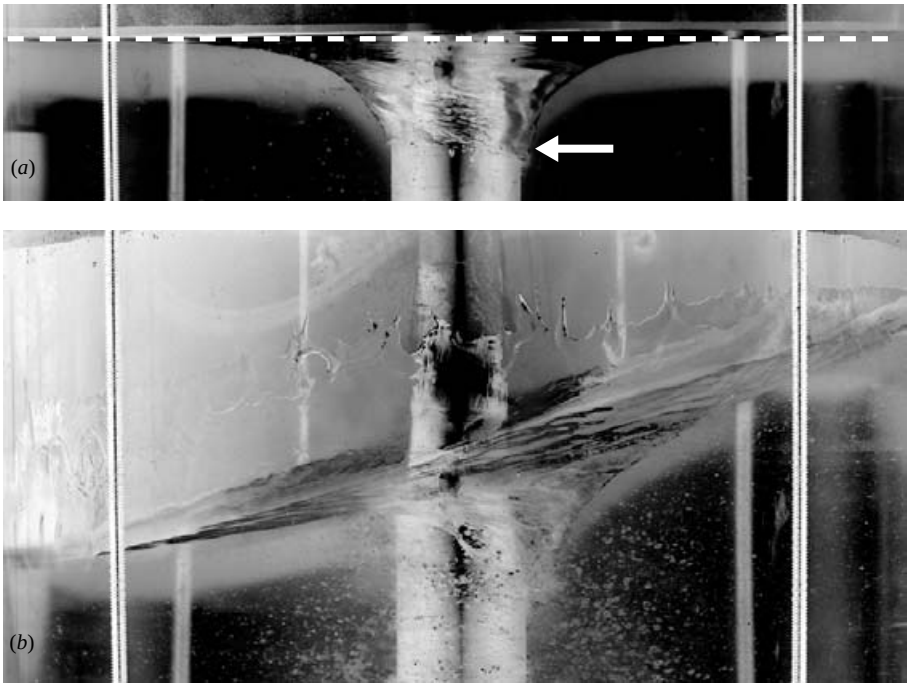

FIGURE 3. (*a*) Base-state surface profile for $F = 20\,\mathrm{Hz}$ ($Re \approx 6.85 \times 10^5$); the surface profiles are fitted to power laws $\eta \sim r^{-\beta}$. For the left- and right-hand side profiles, $\beta_L = 2.0 \pm 0.1$ and $\beta_R = 1.9 \pm 0.1$. The horizontal dashed line shows the height difference between opposite azimuthal angles caused by small-amplitude $m = 1$ waves. The white arrow shows the $m = 1$ spatial perturbation at the inner cylinder. (*b*) A gravity-wave snapshot for $F = 24\,\mathrm{Hz}$ ($Re \approx 8.22 \times 10^5$). The gravity wave corotates with the inner cylinder, counterclockwise viewed from above, at $\approx 1.65\,\mathrm{Hz}$, with a peak-to-peak amplitude of about 12 cm. In both figures $h_o = 50\,\mathrm{cm}$.

not clearly visible in figure 3, but they are when the experiment is visualized from above.

4.2. *Gravity-wave bifurcation*

Close to a critical value F_c^+, where + indicates an increasing rotation rate ramp, surface waves become stronger and more coherent. For the given setup, and for $h_o = 50\,\mathrm{cm}$, we have $F_c^+ \approx 25.2\,\mathrm{Hz}$, which gives a critical Reynolds number $Re_c^+ \approx 8.65 \times 10^5$ (for its definition see the discussion of figure 9*a*). We remark that this value is sensitive to quite small geometrical perturbations, thus care must be taken in order to ensure reproducibility. Above F_c^+, a large-amplitude gravity-wave state sets in (see figure 3*b*), typically after a bifurcation time t_b, which has a statistical nature as will be discussed below. Typically $t_b \sim 7\,\mathrm{min}$, that is about 10000 inner cylinder revolutions (t_b is defined as the time at which the wave growth saturates).

In figure 4 we present representative time series of the normalized wave amplitude $\delta h / h_o$ and normalized dynamic pressure $p_n = (p - \langle p \rangle)/p_{rms}$, where $\langle p \rangle$ and p_{rms} are the mean and root-mean-square (r.m.s.) pressure respectively. The left (resp. right) panel shows time traces below (resp. above) the gravity-wave instability onset. Below onset, the surface disturbance δh presents small-amplitude oscillations, with a fluctuating envelope (figure 4*a*, *c*). The pressure signal is turbulent with fluctuations that are of the order of the pressure r.m.s. value (figure 4*e*). The probability density function (PDF) of both δh and p_n are presented in figure 5. Below onset, these are

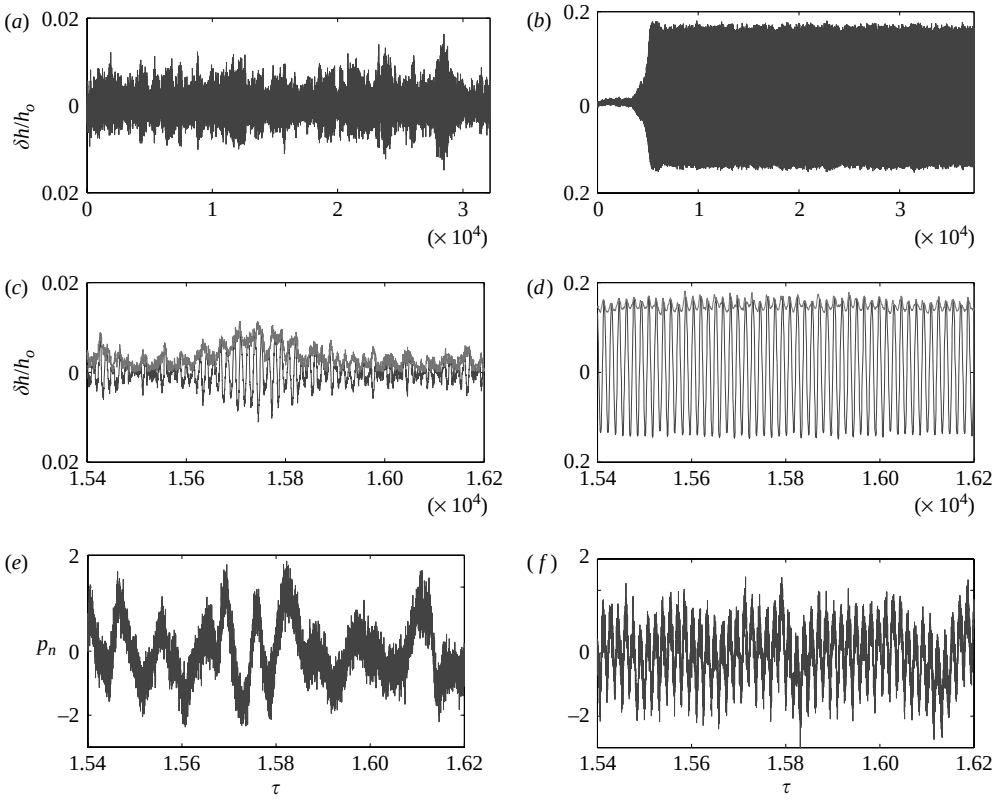

FIGURE 4. Time traces of normalized quantities $\delta h/h_o$ (*a–d*) and $p_n = (p - \langle p \rangle)/p_{rms}$ (*e*, *f*), where p_{rms} is the root-mean-square pressure (in both cases $p_{rms} \approx 155$ Pa). Time is in units of the inner cylinder rotation period ($\tau = tF$). Left (*a*, *c*, *e*) and right (*b*, *d*, *f*) sides correspond to *Re* below and above instability onset respectively; $Re = 7.65 \times 10^5 < Re_c^+$ ($F = 22.34$ Hz), and $Re = 8.86 \times 10^5 > Re_c^+$ ($F = 25.95$ Hz). In (*c*) and (*d*) we present shorter time traces, from (*a*) and (*b*) respectively. Envelope curves are also shown in light grey in (*c*) and (*d*), which are computed from the Hilbert transform of $\delta h/h_o$.

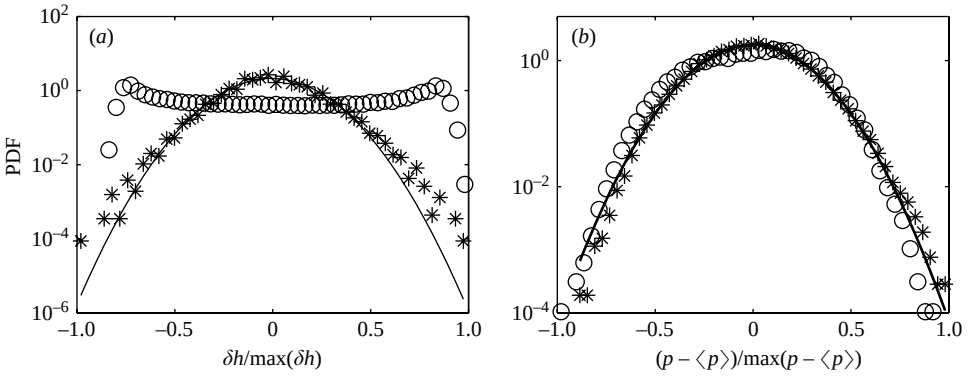

FIGURE 5. Probability distribution functions of (*a*) δh and (*b*) $(p - \langle p \rangle)$, below (∗) and above (○) instability onset, obtained from time series presented in figure 4: $Re = 7.65 \times 10^5 < Re_c^+$ (∗), and $Re = 8.86 \times 10^5 > Re_c^+$ (○) respectively. For reference, solid lines show Gaussian distribution fits to the data below onset.

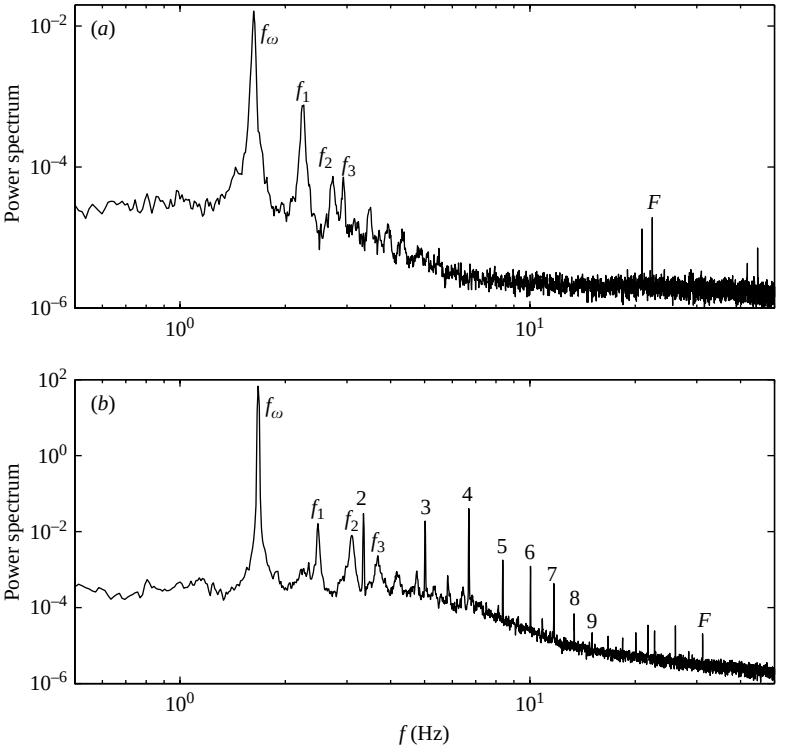

FIGURE 6. Power spectra of δh, below (a) and above (b) instability onset: $Re = 7.65 \times 10^5 < Re_c^+$, and $Re = 1.07 \times 10^6 > Re_c^+$ respectively. The dominant wave frequency is denoted f_w, its harmonics by 2, 3, 4, etc. Other modes are also visible. Those identified by their frequency values in the limit $F \to 0$ are denoted f_1, f_2 and f_3, which correspond to the lower $m = 2$, 0 and 3 modes respectively. Finally, the inner cylinder rotation rate F is also visible.

relatively well fitted by Gaussian distributions, though deviations are detected in the tails.

A typical time trace showing the bifurcation from the turbulent base state to the gravity-wave state is presented in figure 4(b). For the wave state, δh undergoes strong oscillations, as shown in figure 4(d). These oscillations are nonlinear, as evidenced by the presence of harmonics in the temporal Fourier spectrum: at least up to nine harmonics are clearly visible in the power spectrum of δh obtained for $Re = 1.07 \times 10^6$ (figure 6). The envelope of δh in the wave state also fluctuates in time, probably resulting from the flow's underlying turbulence.

Typical Fourier spectra are presented in figure 6, below and above the instability onset. A number of modes are present, and the dominant one is labelled f_w, which corresponds to the lowest $m = 1$ mode. The difference between the main peaks is large. For the data presented in figures 6(a) and 6(b), the energy ratio at f_w is $\approx 6 \times 10^{-4}$. Other modes, labelled f_1, f_2 and f_3, are identified by their behaviour in the limit $F \to 0$. They correspond to the lower $m = 2$, 0 and 3 modes respectively.

A short time series of p_n for the wave state is presented in figure 4(f). It presents oscillations too, also dominated by the free-surface wave frequency f_w. The turbulent fluctuations are, however, of the same order as these oscillations. This is also clear from its probability distribution: the deviation from Gaussian is small, mainly due to some additional flatness around $p \approx \langle p \rangle$, as shown in figure 5($b$). This is unlike

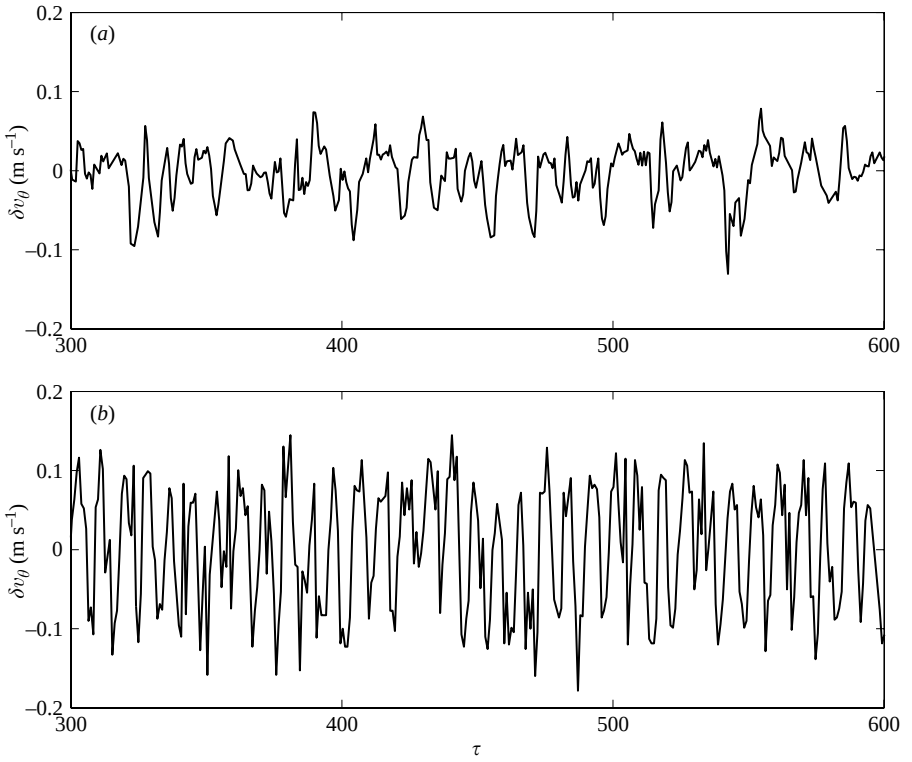

FIGURE 7. Azimuthal velocity time traces $\delta v_\theta = v_\theta - \langle v_\theta \rangle$ at $r = r_o$, below (*a*) and above (*b*) instability onset.

typical probability distributions of δh in the wave state, which deviate strongly from Gaussian, resembling that of a sinusoidal function (see figure 5*a*).

It is important to stress that the observed instability occurs in the entire flow. Both the surface and the bulk of the flow bifurcate from an axisymmetric-dominated mean flow to a non-axisymmetric $m = 1$ flow. The change in the bulk velocity field is seen by simple visual inspection, by following bubble paths. Although we have not fully characterized the bifurcation in the bulk of the flow, we present in figure 7 representative velocity time traces obtained in a different, hybrid setup (see § 5), which also presents this gravity-wave instability. These signals are obtained at the shortest cylindrical radius, $r = r_o$. Note that the represented signal is then the pure azimuthal component. As expected, the oscillations observed in the gravity-wave state (figure 7*b*) are of the same frequency as those observed in both δh and p_n.

For any given rotation rate, temporal Fourier analysis of δh confirms that the dominant frequency is the free-surface gravity-wave fundamental frequency, obtained with $F = 0$, plus a small correction: $f_w = f_o + \delta f(Re)$. Here, f_o is given by the dispersion relation for gravity waves in a fluid layer of finite height h (Landau & Lifshitz 1987): $\omega^2 = gk \tanh kh$, where g is the gravitational acceleration, k the wavenumber, and $\omega = 2\pi f$. For $F = 0$, the fundamental mode is given by a combination of Bessel and Newman cylindrical functions of azimuthal wavenumber $m = 1$. Imposing the appropriate boundary conditions we obtain $k_o = 8.057\,\mathrm{m}^{-1}$. For the oscillations shown in figure 4(*c*), we have $\delta f/f_o \approx 0.13$. Obviously, one should recover $\delta f \to 0$ as $Re \to 0$. In fact, our measurements show that δf follows a power law behaviour for low Re, as shown in figure 8(*b*) below.

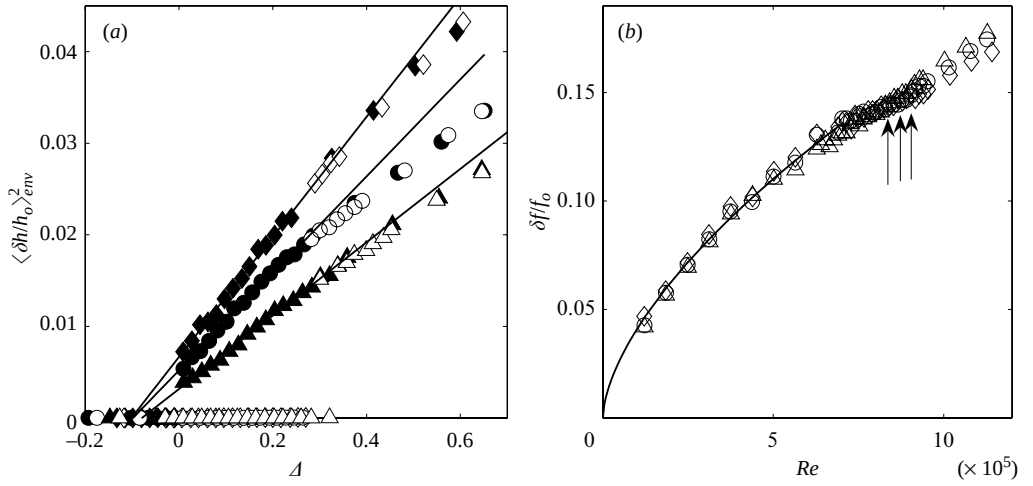

FIGURE 8. (*a*) Bifurcation diagram showing $\langle \delta h/h_o \rangle^2_{env}$ versus $\Delta = (Re - Re_c^-)/Re_c^-$, for $k_o h_o = 2.74$ ($\diamond$), $k_o h_o = 3.38$ ($\circ$), and $k_o h_o = 4.03$ ($\triangle$). Open and solid symbols correspond to increasing and decreasing ramps respectively. Solid lines show linear fits performed in the range $0 \leqslant \Delta \leqslant 0.3$. (*b*) $\delta f/f_o$ versus Re for different water levels h_o (same symbols as in (*a*)). Arrows indicate the approximate Re_c^+ values. The solid line is a fit $\delta f/f_o \sim Re^{\zeta}$ to all the data with $0 < Re < 7 \times 10^5$, which gives $\zeta = 0.62 \pm 0.03$.

Although it is not visible in figure 4(*e*), pressure Fourier spectra also have, in general, a peak at the frequency f_w, which is a signature of the coupling between the pressure field and the oscillations at the free surface. For the data shown in figure 4(*e*), this peak is about 20 dB above the background spectrum. It is worth mentioning that although p_{rms} is approximately the same for the data shown in figures 4(*e*) and 4(*f*), the Fourier-transform pressure peak amplitude ratio is roughly the same as the normalized wave amplitude ratio obtained from the data presented in figure 4(*a*, *b*), as indeed is expected.

The bifurcation diagrams for three different quiescent water levels are plotted in figure 8(*a*). Here we present wave mean-squared amplitude $\langle \delta h/h_o \rangle^2_{env}$, versus the rescaled control bifurcation parameter, $\Delta = (Re - Re_c^-)/Re_c^-$, where Re_c^- is the critical Re value obtained during a decreasing ramp at which the gravity-wave state disappears. (We denote as $\langle \delta h/h_o \rangle_{env}$ the average wave amplitude envelope, that is the average of the light grey curves in figures 4*c* and 4*d*). For each h_o, we observe bistability and hysteresis. In addition, we observe that for small Δ, $\langle \delta h/h_o \rangle^2_{env}$ depends linearly on Δ. Our observations lead us to conclude that the Re values at which the wave state appears depend on the level and form of turbulent fluctuations present in the flow, as well on the distance from $\Delta = 0$. As we control neither the level nor form of turbulent fluctuations we stress that the evidence comes from the generic behaviour we expect for a first-order-type bifurcation (see § 5). The role of fluctuations is, however, less important in the opposite transition obtained during a decreasing ramp, from the wave state to the base state. This is due to the very low probability of having a turbulent fluctuation that would eliminate the high-amplitude gravity wave. The downward transition is then due to the loss of stability of the wave state. The reproducibility in the experimental determination of Re_c^- is high, within $\pm 1\%$. This is unlike the determination of Re_c^+, where a statistical study is necessary (see below). Finally, both Re_c^- and Re_c^+ also vary with h_o (see table 1), which we believe is due

h_o (cm)	$Re_c^- \times 10^{-5}$	$Re_c^+ \times 10^{-5}$
34	7.11 ± 0.07	9.1 ± 0.3
42	6.85 ± 0.07	8.8 ± 0.3
50	6.47 ± 0.07	8.65 ± 0.1

TABLE 1. Values of Re_c^- and Re_c^+ for different quiescent water levels h_o.

to the three-dimensionality of the flow and, possibly, the importance of the axial flow in the instability. However, in terms of the parameter Δ, $\Delta_c^+ \approx 0.3$ seems to be independent of h_o.

In figure 8(b) we show the Re dependence on the normalized surface-wave frequency difference $\delta f/f_o$. The dependence on Re is weak; for $0 < Re < 1 \times 10^6$, f_w only increases about 15% above f_o. Below Re_c^+, this difference scales as $\delta f/f_o \sim Re^{\zeta}$, with $\zeta \approx 0.62$. In this regime, the height dependence is completely determined by the finite height dispersion relation presented previously. However, once the gravity waves set it, we observe a stronger h_o dependence. The fact that f_w is a small correction from f_o allows us to conclude that the instability grows from a resonant mode of the free surface.

5. Discussion and conclusions

The gravity-wave instability observed is clearly a first-order transition: it is not a continuous one and it presents bistability and hysteresis. In the range $0 < \Delta < \Delta_c^+$ the axisymmetric-dominated base-state flow needs a finite-amplitude perturbation in order to bifurcate to the gravity-wave state. A natural question then, is to ask about the role of turbulent fluctuations in the instability. In our system, the fundamental resonant wave mode is always present. In order to grow it needs to get energy from the background turbulent flow. We performed a preliminary statistical study in the bistable region by realizing seven independent increasing rotation rate ramps, over a smaller Re range in the vicinity of Re_c^+. For each Re, we acquired data for a fixed waiting time, $t_w = 24$ min, that is about 35000 inner cylinder rotations. For the same experimental parameters we sometimes observed the gravity-wave onset, such that $t_b < t_w$, and sometimes we did not. The results are summarized in figure 9. Figure 9(a) shows the wave-state probability, which serves precisely to define Re_c^+: for $Re > Re_c^+ = 8.65 \times 10^5$ the measured probability of transiting to the $m = 1$ gravity-wave state approaches one. Figure 9(b) shows the histogram of normalized bifurcation times τ_b for all the six Re values explored in this reduced range. There seems to be a more probable bifurcation time around $\tau_b \approx 10000$, although the distribution is large. A more detailed study of the role of fluctuations at the transition is in progress.

The results presented in figure 9 clearly support the fact that the transition is driven by turbulent fluctuations. We can then speculate about the possibility of describing such a transition by a low-dimensional dynamical system, as previously done by Prigent *et al.* (2002). Assuming that the $m = 1$ wave mode can be described by a time-dependent complex amplitude A, one could try to guess the form of an amplitude equation describing such instability, of the form $\mathrm{d}A/\mathrm{d}t = -\delta\mathscr{F}/\delta\bar{A}$, where $\mathscr{F}$ is the associated Lyapunov potential (Cross & Hohenberg 1993; Prigent *et al.* 2003). Note that stationary solutions are then given by $\delta\mathscr{F}/\delta\bar{A} = 0$, and the stable

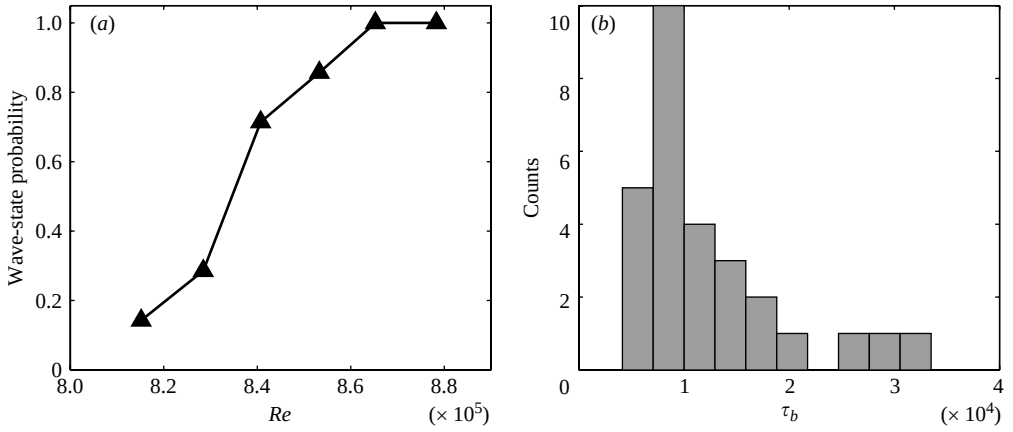

FIGURE 9. (*a*) Measured wave-state probability, obtained from seven independent runs, increasing Re over a reduced range, $Re \approx 815000$–880000 ($h_o = 50\,\mathrm{cm}$). (*b*) Associated normalized bifurcation time histogram ($\tau_b = t_b F$), from which we obtain: median $(\tau_b) = 9576$ and mean $(\tau_b) = 12330$.

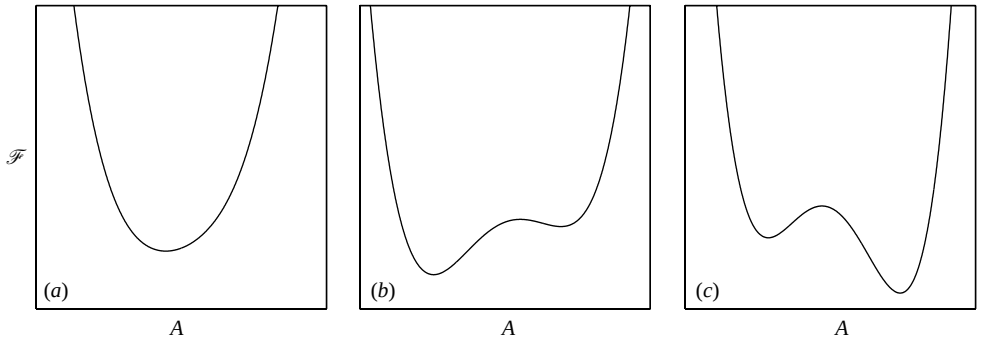

FIGURE 10. Schematic of the expected generic Lyapunov potential $\mathscr{F}$ as function of wave amplitude A, for different ranges of the bifurcation parameter: $\epsilon < 0$ (*a*), $0 < \epsilon < \epsilon_M$ (*b*), $\epsilon_M < \epsilon < \epsilon_c^+$ (*c*). At the Maxwell point, $\epsilon = \epsilon_M$, the two minima are equal. Above ϵ_c^+, there are two possibilities: either $\mathscr{F}$ recovers one minimum, such that the stable solution for the base state (left minimum) and the unstable one (local maximum) disappear through a saddle-node bifurcation, or $\mathscr{F}$ keeps the form shown in (*c*) in a way that the local minimum for the base state never disappears, but only becomes shallower as ϵ increases.

ones correspond to the minima of $\mathscr{F}$. Figure 10 shows the generic expected forms of $\mathscr{F}$, for different values of the bifurcation parameter ϵ. We remark that ϵ is not necessarily equal to the control bifurcation parameter Δ; however, we expect $\Delta = 0 \Rightarrow \epsilon = 0$ and $\Delta = \Delta_c^+ \Rightarrow \epsilon = \epsilon_c^+$. For $\epsilon < 0$ there would be just one minimum associated with the axisymmetric-dominated base state, with small $m = 1$ perturbations driven by turbulence. Between $0 < \epsilon < \epsilon_c^+$ there should be two minima – one for each stable state – which are equal at the Maxwell point $\epsilon = \epsilon_M$. Above ϵ_c^+, the are two possibilities: either $\mathscr{F}$ recovers one minimum, that is the stable solution for the base state (left minimum) and the unstable one (local maximum) disappear through a saddle-node bifurcation; or $\mathscr{F}$ keeps the form shown in figure 10(*c*) such that the local minimum for the base state never disappears, but only becomes shallower as we increase Re, as observed in pipe flow by Hof, Juel & Mullin (2003). In the second

case, for a fixed noise strength, above some Re one would always 'tunnel' into the other state, but with some statistics. In both cases, for $\epsilon > 0$ the role of turbulence is then to trigger the transition from one minimum to the other, passing above a barrier height that becomes smaller and smaller as we increase ϵ. Finally, the asymmetry of the effect of turbulent fluctuations on both transitions observed between the two minima could then be understood if turbulence enters the dynamical equation for A as multiplicative noise.

To end this discussion we present some additional results. We tested the robustness of this instability by performing similar experiments in different geometries: (i) In a smaller hybrid system, composed of an outer 40 cm diameter sphere and a 5.1 cm diameter coaxial inner cylinder we also observed an $m = 1$ transition at $Re_c \approx 4 \times 10^5$, showing bistability and hysteresis. (ii) In the same Taylor–Couette setup but with a larger diameter inner cylinder, of 16 cm radius, we did not observe such transition. By increasing the viscosity ≈ 26 times that of water, using a temperature-controlled water–glycerol mixture, an $m = 0$ corotating gravity-wave state is observed at $Re_c \approx 6 \times 10^4$. Both experiments suggest the crucial importance of the inner-cylinder turbulent boundary layer.

In conclusion, in this paper we report a hysteretic transition of a free-surface Taylor–Couette flow, observed at a very high Reynolds number, $Re_c \sim 10^6$. The base state is statistically axisymmetric respecting the symmetries of the system, whereas the wave state is dominated by a mean flow of azimuthal number $m = 1$. This wave state grows from a resonant mode of the free surface, and it needs the correct perturbation in form and amplitude in order to grow. The energy supply for this wave is probably sourced from the background turbulent flow. We have shown that in the bistable range of the control bifurcation parameter, the gravity wave transition is driven by turbulent fluctuations and that its features can be understood by a generic Lyapunov potential of a complex wave amplitude of the resonant $m = 1$ mode. Finally, the statistics at the transition are probably related to turbulent fluctuations and more work is necessary to fully understand their role.

We thank A. Chen and B. Schwartz for help in some experiments and Don Martin for technical assistance. N. M. acknowledges discussions with Marcel Clerc and support from Chilean grants FONDAP N°11980002 and Fundación Andes N°C-13960. The research was supported by the National Science Foundation of the USA, Condensed Matter Physics and Geophysics programs.

REFERENCES

Billant, P., Chomaz, J.-M. & Huerre, P. 1998 Experimental study of vortex breakdown in swirling jets. *J. Fluid Mech.* **376**, 183.

Coles, D. 1965 Transition in circular Couette flow. *J. Fluid Mech.* **21**, 385.

Cross, M. C. & Hohenberg, P. C. 1993 Pattern formation outside of equilibrium. *Rev. Mod. Phys.* **65**, 851.

Fauve, S. & Pétrélis, F. 2003 The dynamo effect. In *Peyresq Lectures on Nonlinear Phenomena*, Vol. II (ed. J.-A. Sepulchre) pp. 1–64. World Scientific.

Frisch, U. 1995 *Turbulence – The Legacy of A.N. Kolmogorov*. Cambridge University Press.

Hof, B., Juel, A. & Mullin, T. 2003 Scaling of the turbulence transition threshold in a pipe. *Phys. Rev. Lett.* **91**, 244502.

Landau, L. D. & Lifshitz, E. M. 1987 *Fluid Mechanics*. Butterworth Heinemann.

Lathrop, D. P., Fineberg, J. & Swinney, H. L. 1992 Transition to shear-driven turbulence in Couette-Taylor flow. *Phys. Rev. A* **46**, 6390.

Marié, L., Pétrélis, F., Bourgoin, M. *et al.* 2002 Open questions about homogeneous fluid dynamos; the VKS experiment. *Magnetohydrodynamics* **38**, 163.

Pétrélis, F. & Fauve, S. 2001 Saturation of the magnetic field above the dynamo threshold. *Eur. Phys. J. B* **22**, 273.

Prigent, A., Grégoire, G., Chaté, H., Dauchot, O. & van Saarloos, W. 2002 Large-scale finite-wavelength modulation within turbulent shear flows. *Phys. Rev. Lett.* **89**, 164501.

Prigent, A., Grégoire, G., Chaté, H. & Dauchot, O. 2003 Long-wavelength modulation of turbulent shear flows. *Physica D* **174**, 100.

Ravelet, F., Marié, L., Chiffaudel, A. & Daviaud, F. 2004 Multistability and memory effect in a highly turbulent flow: evidence for a global bifurcation. *Phys. Rev. Lett.* **93**, 164501.

Shtern, V. & Hussain, F. 1993 Hysteresis in a swirling jet as a model tornado. *Phys. Fluids A* **5**, 2183.

Shtern, V. & Hussain, F. 1999 Collapse, symmetry breaking, and hysteresis in swirling flows. *Annu. Rev. Fluid Mech.* **31**, 537.

Sisan, D. R., Mujica, N. *et al.* 2004 Experimental observation and characterization of the magnetorotational instability. *Phys. Rev. Lett.* **93**, 114502.

Takeda, Y. 1991 Development of an ultrasound velocity profile monitor. *Nuc. Engng Design* **126**, 277.